Bubble Size Distribution Modeling in Stirred Gas–Liquid Reactors with QMOM Augmented by a New Correction Algorithm

Miriam Petitti, Andrea Nasuti, Daniele L. Marchisio, Marco Vanni, and Giancarlo Baldi
Dipartimento di Scienza dei Materiali e Ingegneria Chimica, Politecnico di Torino, 10129 Torino, Italy

Nicola Mancini and Fabrizio Podenzani
Divisione Refining & Marketing, ENI S.p.a., 20097 S. Donato Milanese, Milan

DOI 10.1002/aic.12003
Published online November 18, 2009 in Wiley InterScience (www.interscience.wiley.com)

Local gas hold-up and bubbles size distributions have been modeled and validated against experimental data in a stirred gas–liquid reactor, considering two different spargers. An Eulerian multifluid approach coupled with a population balance model (PBM) has been employed to describe the evolution of the bubble size distribution due to break-up and coalescence. The PBM has been solved by resorting to the quadrature method of moments, implemented through user defined functions in the commercial computational fluid dynamics code Fluent v. 6.2. To overcome divergence issues caused by moments corruption, due to numerical problems, a correction scheme for the moments has been implemented; simulation results prove that it plays a crucial role for the stability and the accuracy of the overall approach. Very good agreements between experimental data and simulations predictions are obtained, for a unique set of break-up and coalescence kinetic constants, in a wide range of operating conditions.
 AIChE J, 56: 36–53, 2010
Keywords: bubble size distribution, multiphase flow, population balance, gas-liquid stirred tank, quadrature method of moments, moments corruption, moments correction

Introduction

Gas-liquid stirred tank reactors are widely used in chemical, biochemical, pharmaceutical and food industries, and waste-water treatments. In fact, especially under turbulent flow conditions, they are able to provide good gas dispersions and consequently guarantee satisfactory mass and heat transfer characteristics.

Thanks to the increasing computational power, Computational Fluid Dynamics (CFD) is playing a more and more important role in their investigation, design, and scale-up, and it is going to replace traditional methods based on semi-empirical correlations, whose use is limited to geometry and operating conditions similar to those experimentally observed. However, experimental investigations are not completely abandoned as they are needed for model validation; moreover, CFD analysis is used in the chemical industry to direct and optimize the experimental campaign, rather than replace it.

CFD modeling of stirred tanks was initially focused on single-phase liquid flow, and only in the last fifteen years works on multiphase systems started to appear in the literature (a detailed review can be found in Lane[1] and in Gimbun et al.[2]).

In early works,[3–5] the impeller and the baffles were represented by sources/sinks of momentum; steady state simulations were performed in two-dimensional grids under the assumption of axial-symmetry by giving a qualitative

Correspondence concerning this article should be addressed to M. Petitti at miriam.petitti@polito.it.

agreement of the overall flow patterns, but without resolving three-dimensional structures.

Later three-dimensional simulations,[6–11] capable of capturing the actual spatial structures of the flow were carried out, but still modeling the stirrer as a momentum source or by means of boundary condition methods. To overcome these issues, the Sliding-Mesh (SM) and the Multiple Reference Frame (MRF) approaches have been developed.[12,13] Differently from the SM approach, the MRF is a steady-state method and hence is less computationally intensive. When this method is employed the flow is divided into two zones, one rotating with the impeller, whereas the other one is fixed in an inertial reference frame, with information being exchanged at the interface. A good agreement with the experimental velocities was obtained by Luo et al.[14]; the prediction of the trailing vortices, both with the SM and the MRF model was achieved by Wechsel et al.,[13] showing that the MFR approach is a good trade off between accuracy and computational costs.

Another important aspect is the strategy used to describe the multiphase system. In this work we will focus on Eulerian-Eulerian models, where the two phases are described as interpenetrating media through the concept of volume fractions. These methods have been applied to gas–liquid stirrer tanks and were proved to be very promising.[5,8,15,16] Another important issue, deeply investigated in the recent past but still subjected to some controversy, is the treatment of turbulence. Most studies suggest that the Reynolds-Averaged Navier-Stokes approach provides acceptable predictions.[17,18] However, for others like Sun et al.[19] and Wang et al.[20] who employed a k-ε turbulence model in their work, the prediction of the two phase flow was not completely accurate. More sophisticated approaches, such as Direct Numerical Simulation and Large Eddy Simulation, result in more accurate predictions but their computational costs are still quite high for their use on a daily basis for industrial problems and real geometries.[21–23]

Also the role played by the choice of the spatial discretisation method has been investigated and the most significant results are reported in the works by Bakker,[24] Brucato et al.,[25] Aubin et al.,[26] and Luo et al.[27]

Different grid refinement methods have been tested by Deen et al.,[28] who also evaluated the effect exerted by different drag laws, obtaining good predictions for the mean radial velocity, but less accuracy in the description of the gas axial velocity. Scargiali et al.[29] also investigated the effect of grid refinement, and the role played by the turbulent dispersion force, the lift, and virtual mass forces. They concluded that the grid size may have a significant effect on the accuracy of the results, whereas the turbulent dispersion force, lift and virtual mass forces play a secondary role, when compared with the drag force, in determining the distribution of gas hold-up.

Many investigations have been carried out to find proper correlations for the drag force exerted on gas bubbles. Different models, present in literature, considering the rise of a bubble in a stagnant liquid, have been compared,[28,29] but also new correlations have been proposed to take into account the effect of turbulence. Bakker and coworkers[24,30] used a standard drag correlation with a modified Reynolds number, evaluated by means of an effective viscosity, obtained by adding a term proportional to the liquid turbulent viscosity. However, this approach was adopted without reference to experimental data. A new correlation for the drag coefficient in turbulent conditions was then developed by Lane,[31] on the basis of data available in the literature for both solid particles and gas bubbles, showing satisfactory agreement with experimental data.

Another factor that plays an important role in the drag force evaluation and in phase coupling in general, is represented by the correct evaluation of the local bubble size distribution. Most of the works that can be found in literature consider a fixed bubble diameter, but this assumption often represents a significant limitation to a faithful description of gas–liquid reactors which may present strong inhomogeneities in the Bubble Size Distribution (BSD) even under standard operating conditions. This issue was first tackled by Bakker,[24,30] where the assumption of constant and fixed bubble size was abandoned, and the population bubble density model (BDM) was adopted, by using an additional equation for bubble number density, changing for physical transport, break-up, and coalescence, in a one-way coupled approach. Overall gas hold-up and mass transfer coefficient gave satisfactory agreement with experimental data, and also local predictions resulted in acceptable agreement except for the impeller discharge zone. The comparison was however limited to few operating conditions. A similar approach was considered by Djebbar and coworkers[32]: a reasonable agreement was achieved for the global mass transfer coefficient, but comparisons for the internal gas distribution were not performed.

In recent years, the BDM coupled to the CFD has been used to evaluate the local bubble size in gas–liquid stirred tanks by Lane et al.,[31,33] Kerdouss et al.,[34] and Moilanen et al.[35] In most cases, a satisfactory prediction of the local bubble size is achieved, but only by adjusting some of the empirical constants of the model. Besides in the formulation of the BDM proper bubble breakage and coalescence kernels are not included: the equations relative to the bubble size are lumped together and expressed in terms of the critical Weber number and energy dissipation rate without modeling the probability and rate of bubbles collisions and bubble-eddy collisions.

A full Population Balance model, where the bubble size represents the internal coordinate, is thus much preferable. Different methods may be adopted to solve it. In the discretized population balance or classes method (CM) the internal coordinate is discretized into a finite set of bins. In zero-order methods, which are extremely stable, the size distribution is considered constant within each class (or internal coordinate interval), whereas in high order methods (more accurate, but less robust) a specific functional form is assumed. The CM has been used by Muhr et al.[36] for modeling nucleation and crystal growth processes taking place in batch precipitation of photographic emulsions, by Vanni[37] for aggregation-breakage processes with the comparison of different solution procedures, by Venneker et al.,[38] who used the CM with a one-way coupled approach for a stirred tank bioreactor.

Recently, coupled CFD-PBM simulations using the CM have been carried out by Montante et al.[39] presenting a good prediction of the number mean bubble size but a significant

under-prediction of the Sauter mean diameter; by Moilanen et al.,[35] who showed reasonable agreement with the use of fitted constants, and by Kerdouss et al.[40] The major disadvantage of the CM is that it requires a large number of classes to achieve a high level of accuracy, thus needing substantial computational resources.

Good accuracy with a lower computational expense can be achieved by the method of moments. In the Standard Method of Moments (SMM) the internal coordinate is integrated out, and the BSD is determined through its moments,[41] which represent the scalars whose transport equations are solved inside the CFD code. The main advantage of the SMM is that the number of moments required is very small (about 4–6), but it is severely limited by the fact that only size-independent growth rate and the size-independent coalescence/aggregation and breakage kernels can be treated accurately, leading to a closed set of equations.[42]

The ''closure problem'' can be overcome by the Quadrature Method of Moments (QMOM), a method based on the SMM, where the underlying distribution is assumed to be made of delta functions and where, by means of a quadrature approximation, the transport equations of lower-order moments can be written in terms of the lower-order moments themselves. QMOM was first proposed by McGraw[43] for the simulation of aerosol dynamics and then extended and validated for break-up and coalescence problems by Marchisio et al.[44] It results extremely accurate and amenable for coupling with CFD codes, since the local size distribution can be inferred by tracking only a few scalars. For this reason, this method has been chosen in this work for solving the Population Balance Equation (PBE) coupled to CFD, to predict the local bubble size distribution in stirred gas–liquid reactors.

A detailed modeling of two-phase flows via a four-way coupling approach, combining the standard CFD analysis with a Population Balance Modeling (PBM), for taking into account the effect of bubble breakage and coalescence on the bubbles size, has been performed, to estimate the local BSD, key information for the correct evaluation of the specific surface area and the mass transfer rate.

A 194-L baffled gas–liquid reactor, with two different types of spargers, previously investigated by Laakkonen et al.[45,46] with a multi-block model, is studied here with the CFD-PBM model and comparisons with experimental data are carried out in terms of gas hold-up and BSD, both for global and, when available, for local values. The standard Eulerian-Eulerian multi-fluid approach, derived from volume averaging, is adopted here and the PB is solved by resorting to the QMOM, using six moments. One important problem that however has been recently observed in moment transport modeling is the corruption of the moment sets, due to numerical problems of various nature, possibly resulting in nonphysical BSDs in large regions of the domain. This problem, discussed by McGraw[47] and by Wright,[48] has not been widely investigated so far, even if it may compromise seriously the fluid-dynamics and BSD predictions in the reactor, also causing great stability problems in the simulations.

To cope with this issue a great deal of work, in this research, was spent in developing an algorithm to assert the correctness of the moments sequence or to restore them when needed. The method, which relies on the ideas of McGraw[47] and Wright,[48] conferred numerical stability to the simulations, performed for a wide range of operating conditions, leading to good agreement for both global and local features.

Modeling of Multiphase Fluid Dynamics

The approach adopted for describing the fluid-dynamics in the reactors is the Eulerian-Eulerian two-fluid approach, in which both the continuous and the dispersed phases are described by conservation equations written in fixed-coordinates. Each phase is treated as a continuous medium, each interpenetrating the other, identified by its volume fraction (Spalding[49]): α_c is the volume fraction of the continuous liquid phase, whereas α_d is the volume fraction of the dispersed gas bubble phase. Both phases are assumed incompressible. The volume fractions are governed by the following continuity equations (assuming no mass flux between continuous and disperse phase):

$$\frac{\partial}{\partial t}(\alpha_c \rho_c) + \nabla \cdot \left(\alpha_c \rho_c \overline{\mathbf{U}}_c\right) = 0, \tag{1}$$

$$\frac{\partial}{\partial t}(\alpha_d \rho_d) + \nabla \cdot \left(\alpha_d \rho_d \overline{\mathbf{U}}_d\right) = 0, \tag{2}$$

where ρ_c and ρ_d are the densities and where $\overline{\mathbf{U}}_c$ and $\overline{\mathbf{U}}_d$ are the averaged velocities of the continuous and disperse phases, respectively.

These two latter quantities can be calculated by solving the momentum balance equation for the continuous:

$$\frac{\partial}{\partial t}\left(\alpha_c \rho_c \overline{\mathbf{U}}_c\right) + \nabla \cdot \left(\alpha_c \rho_c \overline{\mathbf{U}}_c \overline{\mathbf{U}}_c\right) = -\alpha_c \nabla p + \alpha_c \rho_c \mathbf{g} + \nabla \cdot \mathbf{T}_c + \mathbf{F}_{cd}, \tag{3}$$

and the disperse phase:

$$\frac{\partial}{\partial t}\left(\alpha_d \rho_d \overline{\mathbf{U}}_d\right) + \nabla \cdot \left(\alpha_d \rho_d \overline{\mathbf{U}}_d \overline{\mathbf{U}}_d\right) = -\alpha_d \nabla p + \alpha_d \rho_d \mathbf{g} + \nabla \cdot \mathbf{T}_d - \mathbf{F}_{cd}, \tag{4}$$

where p is the pressure shared by the two phases (surface tension is assumed not to be important as in the cases of nonseparated flows), $\mathbf{g}$ is the gravitational acceleration, $\mathbf{F}_{cd}$ is the interphase force, whereas $\mathbf{T}_c$ and $\mathbf{T}_d$ are the stress strain tensors for the continuous and disperse phase respectively, considering both viscous and turbulent stresses. The last term, written for a generic phase k, results in:

$$\mathbf{T}_k = \alpha_k \left(\mu_{t,k} + \mu_k\right)\left(\nabla \overline{\mathbf{U}}_k + \left(\nabla \overline{\mathbf{U}}_k\right)^T\right), \tag{5}$$

where $\mu_{t,k}$ and μ_k are respectively the turbulent and molecular viscosity for the phase k.

Different turbulent models were tested in preliminary investigations (in which a fixed bubble diameter has been considered) and the one that proved to be a good trade off between accuracy and reasonable computational cost was the k-ε model for the gas–liquid mixture.[50,51] In this approach, the turbulent viscosity in all phases is considered equal to

the turbulent viscosity of the mixture (i.e., $\mu_{t,c} = \mu_{t,d} = \mu_t$) that in turn is defined as follows:

$$\mu_t = \rho_m C_\mu \frac{k^2}{\varepsilon}, \tag{6}$$

where k is the turbulent kinetic energy, ε is the turbulence dissipation rate, ρ_m is the density of the mixture:

$$\rho_m = \alpha_c \rho_c + \alpha_d \rho_d. \tag{7}$$

The turbulent quantities k and ε are calculated by solving specific transport equations:

$$\frac{\partial}{\partial t}(\rho_m k) + \nabla \cdot \left(\rho_m \overline{\mathbf{U}}_m k\right) = \nabla \cdot \left(\frac{\mu_t}{\sigma_k} \nabla k\right) + G_k - \rho_m \varepsilon, \tag{8}$$

$$\frac{\partial}{\partial t}(\rho_m \varepsilon) + \nabla \cdot \left(\rho_m \overline{\mathbf{U}}_m \varepsilon\right) = \nabla \cdot \left(\frac{\mu_t}{\sigma_\varepsilon} \nabla \varepsilon\right) + \frac{\varepsilon}{k}(C_{1\varepsilon} G_k - C_{2\varepsilon} \rho_m \varepsilon), \tag{9}$$

where the production rate of kinetic energy is written as follows:

$$G_k = \mu_t \left(\nabla \overline{\mathbf{U}}_m + \left(\nabla \overline{\mathbf{U}}_m\right)^T\right) : \nabla \overline{\mathbf{U}}_m, \tag{10}$$

$\overline{\mathbf{U}}_m$ is the averaged velocity of the mixture defined as:

$$\overline{\mathbf{U}}_m = \frac{\alpha_c \rho_c \overline{\mathbf{U}}_c + \alpha_d \rho_d \overline{\mathbf{U}}_d}{\alpha_c \rho_c + \alpha_d \rho_d}. \tag{11}$$

The constants used in the model are those generally employed for single phase turbulence (i.e., $C_\mu = 0.09$, $C_{1\varepsilon} = 1.44$, $C_{2\varepsilon} = 1.92$, $\sigma_k = 1.0$, and $\sigma_\varepsilon = 1.3$). Standard wall functions were used to characterise turbulence-wall interaction.

Only the drag contribution is considered for the interface force, as in stirrer tanks is the controlling one (on the contrary on what happens in bubble columns where other forces are also relevant). The force can be written as follows (Ishii and Zuber[52]; Tomiyama[53]):

$$\mathbf{F}_{cd} = \frac{3}{4} \rho_c \alpha_d \frac{C_D}{d_b} \left|\overline{\mathbf{U}}_d - \overline{\mathbf{U}}_c\right| \left(\overline{\mathbf{U}}_d - \overline{\mathbf{U}}_c\right), \tag{12}$$

where C_D is the drag coefficient, and d_b is the bubble diameter. When in each point of the reactor an actual BSD exists d_b can be calculated as the area-averaged bubble size or Sauter diameter, d_{32}. Of course, the accuracy of this approximation decreases as the BSD widens. When the BSD is very wide (as it may occur for example in bubble columns operated in the heterogeneous regime) this approach may become inaccurate and an interesting alternative is to represent the population of bubbles as constituted by several dispersed phases, each characterized by specific volume fraction, velocity, and size. The closure needed for the evaluation of the drag coefficient C_D can be formulated in terms of the terminal velocity of the bubbles U_∞ by employing for example the following equation:

$$C_D = \frac{4 d_b (\rho_\mathrm{c} - \rho_\mathrm{d})\mathrm{g}}{3 \rho_\mathrm{c} U_\infty^2}, \tag{13}$$

where the bubble size can again be evaluated through the local area-averaged bubble size (d_{32}) and where details concerning the choice of the terminal velocity are given in the next sections.

Population Balance Modeling

An important aspect that often needs to be modeled is the BSD change due to bubble coalescence and breakage, with a possible significant impact on local values of velocity profiles, gas volume fraction, and interfacial area. For this purpose, a PBE can be coupled with the multi-fluid description by resorting to the procedure reported in the next section.

The equations coupled with the two-fluid model, used to describe the bubble size evolution, derive from the Generalized Population Balance Equation (GPBE) that is a continuity statement written in terms of a Number Density Function (NDF), as explained by Fox.[54] The NDF is in turn a smooth and differentiable average function of the disperse phase, that, according to the following expression, gives the expected number of elements (in this case bubbles) in the physical volume $d\mathbf{x} = dx_1 dx_2 dx_3$ around the point $\mathbf{x} = (x_1; x_2; x_3)$ and with bubble size in the range $(L, L + dL)$:

$$n(L; \mathbf{x}, t)\mathrm{d}\mathbf{x}\mathrm{d}L. \tag{14}$$

This BSD is governed by the PBE that can be obtained from the GPBE and for the case under investigation can be written as follows:

$$\frac{\partial}{\partial t}[n(L)] + \nabla \cdot \left[\overline{\mathbf{U}}_d n(L)\right] = [B(L; \mathbf{x}, t) - D(L; \mathbf{x}, t)], \tag{15}$$

where $\overline{\mathbf{U}}_d$ is average velocity of the bubbles calculated from Eq. 4 while $B(L, \mathbf{x}, t)$ and $D(L, \mathbf{x}, t)$ represent the birth and death rates of bubbles with size L owing to breakage and coalescence. Time and space dependencies will be omitted in what follows.

The overall birth and death terms are given by the summation of the birth and death terms relative to breakage and coalescence. The birth term due to breakage is:

$$B^B(L) = \int_L^\infty \beta(L, \lambda) g(\lambda) n(\lambda) d\lambda, \tag{16}$$

whereas the birth term due to coalescence is:

$$B^C(L) = \frac{1}{2} \int_0^\infty h\left(\left(L^3 - \lambda^3\right)^{1/3}, \lambda\right) n\left(\left(L^3 - \lambda^3\right)^{1/3}\right) n(\lambda) d\lambda, \tag{17}$$

The death terms due to breakage and coalescence read as follows:

$$D^B(L) = g(L) n(L), \tag{18}$$

$$D^C(L) = \int_0^\infty h(L,\lambda)n(L)n(\lambda)d\lambda. \tag{19}$$

The coalescence kernel $h(L, \lambda)$ represents the frequency of coalescence of two bubbles of size L and λ, whereas $g(L)$ is the breakage kernel, that is the frequency of break-up of a bubble of size L; $\beta(L,\lambda)$ is the daughter distribution function, the BSD of bubbles formed by the break-up of a bubble of size λ.

The kernels adopted to describe the frequency of bubbles breakage and coalescence are those presented by Laakkonen et al.[45] in their work and were derived from the theory of turbulence applied to multiphase disperse systems. According to this theory, the frequency of bubbles breakage can be expressed as the product of the frequency with which turbulent eddies in the liquid phase collide against the bubble surface and the probability that such a collision leads to bubble break-up. The underlying hypotheses for the kernels used in this work are that turbulence is isotropic, that the size of fluid particles is in the inertial subrange and that break-up is induced by collisions with turbulent eddies smaller than or with the same size of the bubble, characterized by energy levels above a critical threshold.

The expression for the break-up kernel, employed in this work, was developed by Narsimhan et al.[55] to describe the break-up of droplets, assuming the arrival of eddies on the surface of a droplet as a Poisson process. Later this expression was modified by Alopaeus et al.[56] that inserted the dependence on $\varepsilon^{1/3}$ in the eddy collisions frequency and the viscous stresses in the energy balance, considered in the probability for a collision to turn into break-up. Finally, Laakkonen et al.[45] used this kernel to describe bubble break-up, considering the fact that the mechanism of break-up of drops and bubbles are closely related. They further modified its expression by replacing the disperse phase viscosity with the continuous phase viscosity, considering that one component of the forces opposing bubble break-up is given by the viscous stresses of the surrounding liquid. The final expression of the break-up kernel follows:

$$g(L) = C_1\varepsilon^{1/3}\mathrm{erfc}\left(\sqrt{C_2\frac{\sigma}{\rho_c\varepsilon^{2/3}L^{5/3}} + C_3\frac{\mu_c}{\sqrt{\rho_c\rho_d}\varepsilon^{1/3}L^{4/3}}}\right). \tag{20}$$

Among all the possible choices, this expression was used because it leads to the best agreement with experimental data, although some theoretical issues related to its final functional form still needs to be addressed. In fact, it appears that the constant C_1 has the dimension of length to the minus two third and, according to the theory, should be linked to an integral length-scale in the vessel. This means that C_1 is not a true kinetic constant, but it contains some scaling parameter; great care should be taken when employing this expression to reactors with very different geometrical characteristics. There is no reliable way to calculate a priori C_1, therefore, its value was determined from a fitting procedure by comparison with experimental data and by considering a wide range of operating conditions. For C_2 and C_3 the values adopted by Laakkonen et al.[45] were considered: 0.04 and 0.01, respectively.

The expression adopted for the daughter distribution function is based on the work of Laakkonen et al.[45] and considers binary break-up, since it is the most common in the case of gas bubbles. It assumes that two bubbles of different sizes are formed in the break-up process, owing to the gas redistribution mechanism, caused by external stresses, as described in detail by Andersson and Andersson.[57] The final functional form for the daughter distribution function is given by:

$$\beta(L,\lambda) = 180\left(\frac{L^2}{\lambda^3}\right)\left(\frac{L^3}{\lambda^3}\right)^2\left(1-\frac{L^3}{\lambda^3}\right)^2, \tag{21}$$

where L is the size of the daughter bubble generated by the break-up of a "mother bubble" of size λ.

The coalescence phenomenon instead can be reasonably summarized in three consecutive steps: bubbles approach because of turbulent fluctuations, drainage of the liquid film trapped between the bubbles and their final union. The controlling step is considered the liquid film drainage: it is assumed that coalescence can take place only if colliding bubbles remain in contact for sufficient time so that the liquid film trapped between them, drains out until a critical thickness is reached; in this process, an important role is played by surfaces mobility. The expression used for the coalescence kernel derives from the model of Coulaloglou and Tavlarides[58] for the collision frequency, where a small algebraic correction is made[59–61]:

$$h(\lambda,L) = C_7\varepsilon^{1/3}(\lambda+L)^2\left(\lambda^{2/3}+L^{2/3}\right)^{1/2}\eta(\lambda,L). \tag{22}$$

The first part of the kernel represents the frequency of collision between two bubbles and this expression is calculated from the kinetic gas theory, where $\lambda + L$ represents the diameter of the collision cross section. A theoretical value of the parameter C_7 exists for stirred reactors and is equal to 0.88.[38]

The second part of the kernel instead represents the efficiency of coalescence of two colliding bubbles and this expression is evaluated considering the liquid drainage as controlling step and the bubbles deforming with immobile surfaces, according to Coulaloglou and Tavlarides[58]:

$$\eta(\lambda,L) = \exp\left(-C_8\frac{\mu_c\rho_c\varepsilon}{\sigma^2}\left(\frac{\lambda L}{\lambda+L}\right)^4\right). \tag{23}$$

The initial and the final critical thickness of the liquid film between the bubbles are assumed constant and are considered in the model through the parameter C_8. In this model, the force compressing the bubble is assumed proportional to the mean-square velocity difference at the ends of the fluid eddy of size $\lambda + L$.

Numerical Solution with QMOM, Moments Sets Corruption, and Correction Algorithm

When using QMOM the PBE (Eq. 15) is written in terms of the moments of the BSD, where the generic kth moment of the BSD is defined as follows:

$$m_k = \int_0^\infty n(L) L^k dL. \tag{24}$$

Lower order moments are very important since they correspond to specific physical properties of the distribution. For example, m_0 represents the total number of bubbles per unit volume of the system considered, m_1 their total length, m_2 is linked to their area by means of the area shape factor k_A, whereas m_3 is related to their volume through the volume shape factor k_V. Moreover, the area-averaged bubble size (i.e., Sauter diameter) is defined as the ratio between the moments of order three and two:

$$d_{32} = \frac{\int_0^\infty L\, n(L) k_A L^2 dL}{\int_0^\infty n(L) k_A L^2 dL} = \frac{m_3}{m_2}. \tag{25}$$

The final moment transport equation reads as follows:

$$\frac{\partial m_k}{\partial t} + \nabla \cdot \left[\overline{\mathbf{U}}_d^k m_k \right] = [\bar{B}_k - \bar{D}_k] \tag{26}$$

where $\overline{\mathbf{U}}_d^k$ is the velocity of the moment of order k, that is theoretically different for each moment of the BSD. Since in this work a unique bubble velocity is calculated, $\overline{\mathbf{U}}_d^k$ is taken to be the same for all moments and equal to $\overline{\mathbf{U}}_d$ calculated from Eq. 4. The source terms, due to bubble break-up and coalescence evaluated for the moments, are:

$$\begin{aligned} &\bar{B}_k - \bar{D}_k \\ &= \frac{1}{2} \int_0^\infty n(L) \int_0^\infty h(L,\lambda) \left[\left(L^3 + \lambda^3\right)^{k/3} - L^{k/3} - \lambda^{k/3} \right] n(\lambda) d\lambda dL \\ &+ \int_0^\infty L^k \int_0^\infty g(\lambda) \beta(L,\lambda) n(\lambda) d\lambda dL - \int_0^\infty L^k g(L) n(L) dL \end{aligned} \tag{27}$$

The difficulty is now represented by the evaluation of these source terms, expressed as integrals of the BSD. This closure problem is overcome by resorting to a quadrature approximation of order N_d defined through its N_d weights w_i and nodes (or abscissas) L_i that in turn can be calculated from the first $2N_d$ moments by resorting to a very stable and efficient algorithm [i.e., the Product-Difference (PD) algorithm, see Gordon[62] for details]. If the quadrature approximation is applied the source term for the generic moment m_k becomes:

$$\begin{aligned} \bar{B}_k - \bar{D}_k = &\sum_{i=1}^{N_d} g(L_i) w_i \bar{\beta}_i^k - \sum_{i=1}^{N_d} L_i^k g(L_i) w_i \\ &+ \frac{1}{2} \sum_{i=1}^{N_d} w_i \sum_{j=1}^{N_d} w_j \left(L_i^3 + L_j^3 \right)^{k/3} h(L_i, L_j) \\ &- \sum_{i=1}^{N_d} L_i^k w_i \sum_{j=1}^{N_d} h(L_i, L_j) w_j, \end{aligned} \tag{28}$$

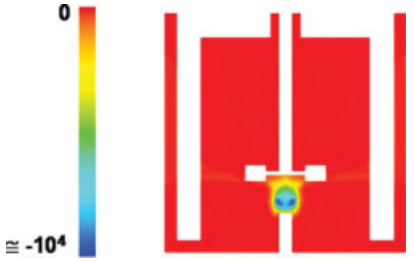

Figure 1. Moment of order 2 predicted by a simulation in which the correction algorithm is not applied.

Zones with negative values can be observed. [Color figure can be viewed in the online issue, which is available at www.interscience.wiley.com.]

where $\bar{\beta}_i^k$ is the integral:

$$\bar{\beta}_i^k = \int_0^{L_i} L^k \beta(L_j, L_i) dL_j. \tag{29}$$

An analytical solution exists in the case of binary break-up ($C_4 = 2$) and with $k \geq 0$:

$$\begin{aligned} \bar{\beta}_i^k &= \int_0^{L_i} 2 \cdot L_j^k \cdot 90 \left(\frac{L_j^2}{L_i^3} \right) \left(\frac{L_j^3}{L_i^3} \right)^2 \left(1 - \frac{L_j^3}{L_i^3} \right)^2 dL_j \\ &= \frac{3240 \cdot L_i^k}{(k+9)(k+12)(k+15)}. \end{aligned} \tag{30}$$

Although all the results reported here correspond to the binary case (i.e., $C_4 = 2$) other values were also tested and for these other values a numerical integration must be carried out. The numerical integration can be carried out by resorting to a quadrature formula that uses fixed and equi-spaced nodes (Newton-Cotes) or to a quadrature approximation with fixed and nonequi-spaced nodes, coinciding with the zeros of proper polynomials (Gaussian formula). These two methods have been compared, and the results obtained with the Gaussian approximation showed better accuracy. In particular, the Gauss-Legendre quadrature approximation with seven nodes resulted in a final relative error smaller than 10^{-5}.

In this research QMOM, with $N_d = 3$ is adopted and is calculated by tracking the first six moments (i.e., from m_0 to m_5) of the BSD. The use of three nodes was proven to give an acceptable approximation of the solution for these kind of kernels.[63] From the physical point of view these moments are linked by proper relationships, since representing different characteristics of the same BSD, but the numerical resolution of their independent transport equations cannot guarantee the preservation of these relationships.

In fact, very often their relationships are altered by the discretisation schemes used by the CFD code (especially higher-order schemes) and invalid moment sets are created in the reactor (Figure 1), that is to say sets of moment no longer representative of physical BSDs. A phenomenon that accompanies the creation of the corrupted moment sets is the loss of numerical stability in the simulation: high peaks

Table 1. Example of Difference Table for the Convexity Test of a Moment Set (Valid)

k	ln (m_k)	d_1	d_2	d_3	d_4	d_5
0	0	1	2	0	0	0
1	1	3	2	0	0	–
2	4	5	2	0	–	–
3	9	7	2	–	–	–
4	16	9	–	–	–	–
5	25	–	–	–	–	–

are observed in the residuals of the scalars associated to the moments, until the simulation diverges completely.

For this reason great attention has been directed to the development of a test algorithm to assess the validity of a moment set, and of a correction method, in case an invalid set is encountered. The validity of the generic moment set is checked by assessing the positivity of the following determinants derived from the moments:

$$\Delta_{n,l} = \begin{vmatrix} m_n & m_{n+1} & \dots & m_{n+l} \\ m_{n+1} & m_{n+2} & \dots & m_{n+l+1} \\ \vdots & \vdots & \vdots & \vdots \\ m_{n+l} & m_{n+l+1} & \dots & m_{n+2l} \end{vmatrix} \geq 0, \qquad (31)$$

for $n = 0, 1$ and $l \geq 0$. This condition, for the first four moments of the BSD (m_0, m_1, m_2, m_3) is equivalent to the convexity check of the natural logarithm of m_k as a function of k:

$$m_k m_{k-2} - m_{k-1}^2 \geq 0. \qquad (32)$$

Details are reported in Appendix A and here a brief summary is presented. If ln(m_k) is convex the set of moments is valid, otherwise it is corrupted and needs to be restored. In practice, the difference table of the function ln(m_k) is built, and this condition is checked by assessing that all the elements of the column relative to the second differences are positive (Tables 1 and 2, where the test is carried out for two sets, the first one being valid and the second one non-valid). If the moment set results valid, no correction is performed, and the moments are directly used to evaluate the nodes and weights for the estimation of the source terms, by means of the PD algorithm, otherwise the set is corrected, before being passed to the PD algorithm.

The method adopted for recovering invalid moments sets is the Minimum Square Algorithm developed originally by McGraw[47]; it is an iterative method based on the idea of identifying and correcting only the moment of index k^* which after adjustment maximizes the smoothness of the function ln(m_k), through a minimization procedure. The method,

Table 2. Example of Difference Table for the Convexity Test of a Moment Set (Non-valid)

k	ln (m_k)	d_1	d_2	d_3	d_4	d_5
0	0	1	2	−3	12	−30
1	1	3	−1	9	−18	–
2	4	2	8	−9	–	–
3	6	10	−1	–	–	–
4	16	9	–	–	–	–
5	25	–	–	–	–	–

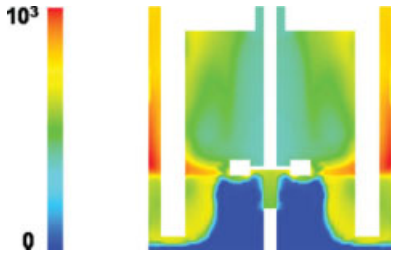

Figure 2. Moment of order 2 predicted by a simulation in which the correction algorithm is applied.

Zones with negative values are not observed any longer and all values are now physically consistent. [Color figure can be viewed in the online issue, which is available at www.interscience.wiley.com.]

described in Appendix A, in a few iterations identifies the index k^* of the moment that must be corrected, as well as the corrected value of the moment that results in a valid set.

Sometimes, however, this method does not succeed in correcting the moments set in an acceptable number of iterations, and therefore, after some iterations are carried out, a second correction procedure is implemented in cascade. This second method, proposed by Wright,[48] consists in restoring the corrupted moment sequence with the moments calculated as the arithmetic mean of those of two log-normal distributions. The distributions are evaluated from the first four moments of the set that must be corrected, keeping fixed m_0 and m_3, which are related to the number of bubbles per unit volume and their volume fraction, respectively. Details are reported in Appendix B.

Both algorithms play a crucial role in the simulation, allowing the correction of the unphysical results typical of moment corruption, such as negative nodes and negative moments throughout the reactor (Figures 1 and 2) and the removal of the associated stability problems. As a matter of fact, the correction algorithms mainly act only on higher order moments (higher than m_3), that are not fed back to the CFD code; moreover, the magnitude of correction is quite small, thus the algorithms do not alter significantly the final solution, but confer higher stability to the code and make possible the use of much higher under-relation factors for the moments.

Operating Conditions, Simulation Settings, and Numerical Details

The reactor investigated in this work is a 194-liter four-baffled reactor, agitated by a six-blade Rushton turbine and with a gas sparger below the impeller. Two different spargers are considered: a circular metal porous sparger with diameter of 3.3 cm and pores of 15 μm, located 10.5 cm below the impeller and used for low gassing rates, and a ring sparger with mean diameter of 10 cm and 12 holes of 2 mm, placed 15.5 cm below the impeller, suitable for higher hold-ups. These particular configurations were already investigated by Laakkonen et al.,[45,46] and detailed experimental measurements are available for model validation. In Figure 3a–c the vessel dimensions are reported as well as the points in which experimental measurements were carried out for the two gas sparger configurations. The continuous

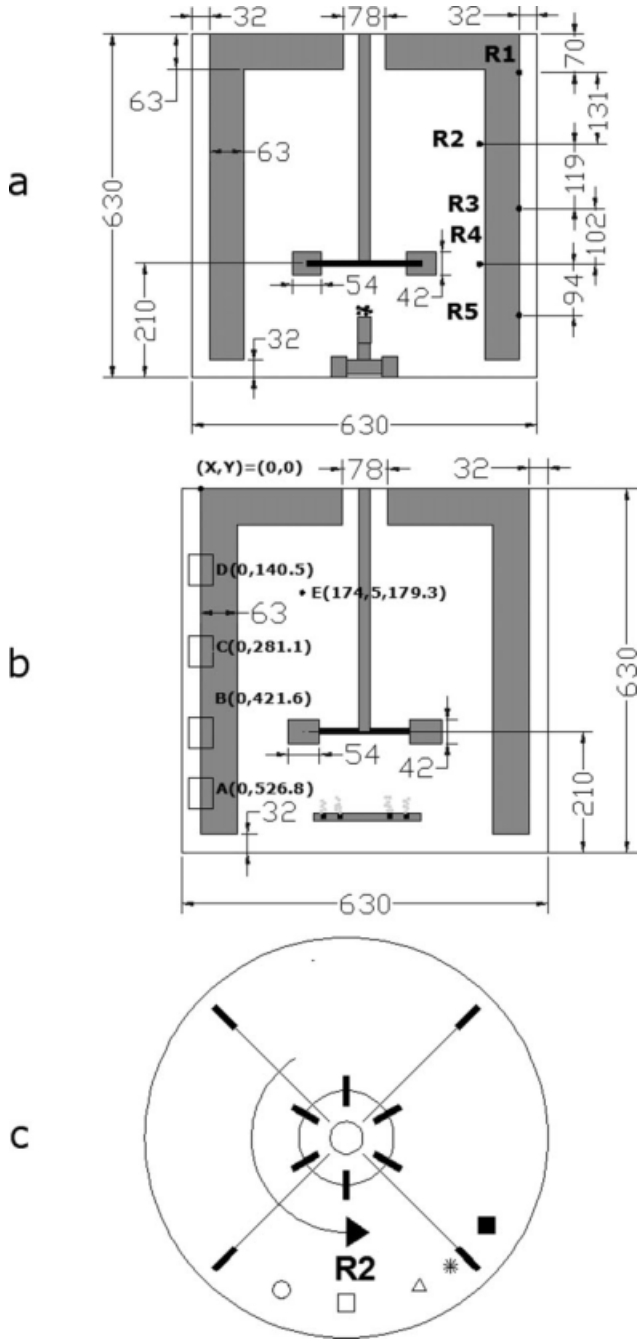

Figure 3. Side views of the porous sparger reactor (a), the ring sparger reactor (b), and the top view (c) of both reactors.

The axial points for which experimental data are available for both the porous sparger and the ring sparger configuration are marked.

liquid phase is water, and the dispersed gaseous phase is air; the properties used in the simulations are the followings: $\rho_{water} = 998.2$ Kg/m^3, $\mu_{water} = 1 \times 10^{-3}$ Pa s, $\rho_{air} = 1.225$ Kg/m^3, $\mu_{air} = 1.78 \times 10^{-5}$ Pa s.

For the reactor with the porous sparger the predicted BSDs were compared with the experimental ones in the measurement points for a wide range of operating conditions. The stirring rate ranged between 155 and 250 rpm, and the gas flow rate ranged from 0.018 to 0.093 volume of gas per volume of reactor per minute (vvm), resulting in global hold-up values up to 1.5%. The operating conditions investigated are reported in Table 3. Also for the reactor with the ring sparger, model validation was carried out in a wide range of operating conditions (i.e., 390 rpm, 0.1–1 vvm, hold-up up to 7%, as reported in Table 4). However, in this case only experimental global hold-up values were available in all the operating conditions, whereas the detailed comparison of the BSD was possible only at 390 and 0.7 rpm.

Table 3. Operating Conditions Investigated for the Reactor with the Metal Porous Sparger

Stirring speed (rpm)	Gassing rate (vvm)
155	0.018
155	0.041
157	0.052
220	0.018
220	0.041
250	0.052
250	0.072
250	0.093

The simulations were carried out with the MRF approach and were performed by considering one half of the geometry, since this is the smallest portion of the reactor that satisfies the conditions of geometrical symmetry and of periodicity. A number of hexahedral cells between around 230,000 for meshing the reactor were found to be sufficient to characterize the bulk flow field, since both the flow and the power number did not show significant change with further grid refinement.

The computational grids were created by using Gambit, whereas simulations were performed with the commercial code Fluent 6.2 and User-Defined Functions and Subroutines were used to implement the PBM, the drag model, the correction, and PD algorithms. The transport equations for the moments were solved by defining six additional scalars for the dispersed gaseous phase (details can be found in Appendix C).

As already reported a closure is needed for the calculation of the terminal velocity used in Eq. 13 to compute the drag force. This closure should take into account the effect of bubble size and shape, turbulence intensity as well as the effect of the presence of other surrounding bubbles (i.e., swarm effect). It is important to remind here that in this work a unique internal coordinate was used in the PBM so

Table 4. Operating Conditions Investigated for the Reactor with the Ring Sparger

Stirring speed (rpm)	Gassing rate (vvm)
390	0.1
390	0.25
390	0.4
390	0.5
390	0.6
390	0.7
390	0.8
390	0.9

all the bubbles are assumed to be spherical, a reasonable assumption in the investigated bubble size range (i.e., between 2 and 10 mm); moreover, this bubble size range is consistent with the choice of a unique value for the terminal velocity for all the bubbles. An isolated air bubble, included in the considered size range (corresponding to the plateau region of Mendelsons' law[65]) and rising in still water presents a terminal velocity of about 26 cm/s, but this value must be corrected to take into account the effect of turbulence, as suggested by Montante et al.[66] The effect of turbulence on the value of bubbles terminal velocity was studied in a previous work,[51] where a modified Bakker's correction was proposed: different values of the fitting constant of Bakker's correction were tested and good agreement with empirical correlations, and experimental data was achieved for those corresponding to a bubble terminal velocity of 12–13 cm/s about. Although this correction should be applied and calculated with the local turbulence intensity and gas hold-up, in this work a simplified approach was used, and a constant terminal velocity of 13 cm/s was adopted throughout the entire reactor.

Moreover, at very high hold-ups (above 5%) the value needs to be further corrected to consider the effect exerted by the interactions of the bubbles on their rising velocity. When the hold-up increases coalescence is promoted, as predicted by the kernel considered in the model, and bubble size increases, but this fact, in the systems considered, does not alter their velocity since the bubbles are still included in the size range mentioned before. Instead their increased concentration causes interactions between them, which interfere with their rising motion, leading to a lower terminal velocity. Extensive validation based on comparison with correlations derived from experimental data resulted in a further reduction to about 8.5 cm/s.[51] Therefore, a terminal velocity of 13 cm/s, throughout the entire reactor, was considered for global hold-ups smaller than 5% and of 8.5 cm/s for global gas hold-ups larger than 5%. The issue of reliable closure drag laws, far from being completely addressed in this work, will be further investigated in our future work.

As far as the boundary conditions are concerned, the section of the sparger from which the gas is introduced in the reactor was defined as a velocity inlet. On this velocity inlet the gas volume fraction was evaluated as the geometrical area portion available for gas passage and then, by knowing the gas volumetric flow rate, the gas velocity was determined. The liquid velocity components were set null. The upper surface of the liquid was defined as a pressure outlet to let the gas exit from the system and, if there is a backflow, it is formed by liquid only.

The moments associated with the inflowing gaseous dispersed phase on the velocity inlet section were prescribed on the basis of bubbles inlet distribution. For the porous sparger, the inlet BSD was modeled as a log-normal distribution assuming that the standard deviation is 15% of the mean bubble size, as usually observed with metal porous spargers, and with a mean bubble size at the inlet ($d_{b,inlet}$) calculated with the correlation proposed by Kazakis et al.[67]:

$$d_{b,inlet} = 7.35\left[\mathrm{We}^{-1.7}\mathrm{Re}^{0.1}\mathrm{Fr}^{1.8}\left(\frac{d_p}{d_s}\right)^{1.7}\right]^{1/5} \quad (33)$$

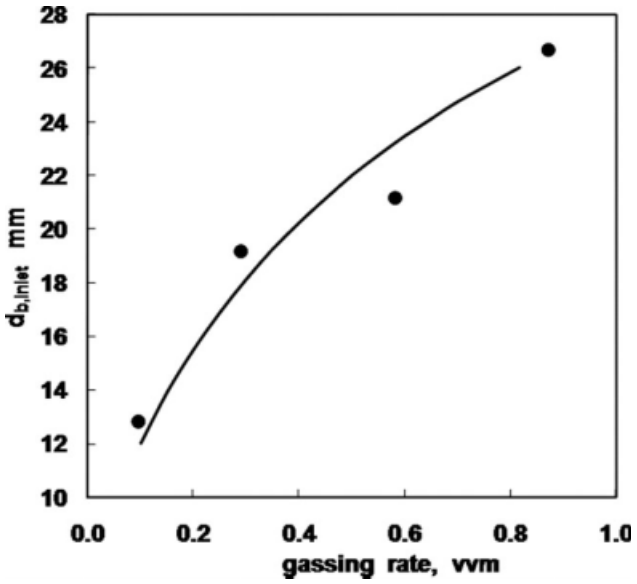

Figure 4. Comparison between calculated and experimentally measured mean bubble size exiting the ring sparger as a function of the gassing rate.

Continuous line: predictions from the model of Geary and Rice[52]; symbols: experimental values measured by Laakkonen et al.[53]

where We, Re, Fr are Weber, Reynolds, and Froude dimensionless numbers, whose definition is reported in the original work of Kazakis et al.,[67] and where d_p and d_s are the pore diameter and the sparger diameter, respectively. In the case of the ring sparger, a normal distribution was assumed, with the mean diameter evaluated according to Geary and Rice,[68] that presents a two step growth of the entering bubble, and a standard deviation calculated as a function of $d_{b,inlet}$, as suggested by Laakkonen et al.[46] As an example, the inlet mean bubble size calculated for the ring sparger for different gassing rates is shown in Figure 4 as a function of the inlet gas flow rate.

Results and Discussion

The algorithm developed to cope with the problem of moments numerical corruption has proved to play a crucial role in the simulations. When no correction was applied in conjunction with the use of higher-order spatial discretization schemes, unphysical results, such as negative moments, were observed, in confined zones (often one of them coinciding with the sparger zone, as in Figure 1) or throughout the reactor, and stability problems were encountered during the simulation. Instead the implementation of the correction algorithm managed to guarantee numerical stability and prevented moments corruption (see for example Figure 2), without changing the final solution. Therefore, the correction algorithm developed is capable to make robust, against the problem of moments corruption, the QMOM method, which can be as accurate as the CM in the BSD prediction, but results far less computationally demanding, and so makes feasible its coupling with the CFD code, as done in this

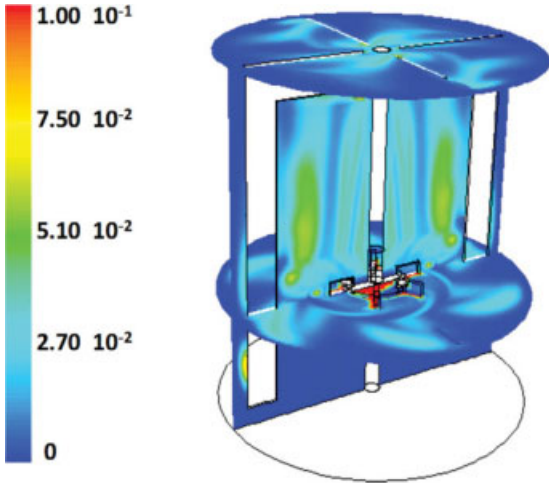

Figure 5. Gas volume fraction predicted by the CFD simulation on an axial plane and on two tangential planes, in the reactor with the porous sparger at 250 rpm and 0.093 vvm.

[Color figure can be viewed in the online issue, which is available at www.interscience.wiley.com.]

work. The CM instead, owing to its high computational cost, was used by Laakkonen et al.[45,46] in conjunction with a multi-block model, that gives a less detailed description of the fluid-dynamic with respect to a complete CFD model.

As already reported, the results presented and discussed in what follows focus on the predictions of gas distribution profiles, global hold-up and BSD, and their comparison with experimental data from the literature[45,46] and with predictions obtained from empirical correlations based on experimental investigations. In the numerical simulations, the residuals of all the quantities have been monitored and used as criterion for convergence. The residuals of the simulations carried out on the porous sparger reactor stabilized at 10^{-6} about, whereas those relative to the simulations of the ring sparger reactor at 10^{-4} about.

Let us first analyze the results obtained with the porous sparger. The gas distribution predicted by the simulation for

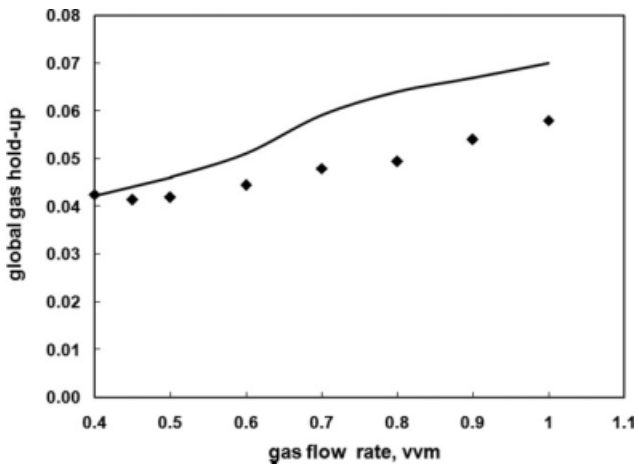

Figure 6. Comparison of the global hold-up values predicted by the CFD simulation with the experimental data, for the reactor with the ring sparger, at 390 rpm and different gassing rates.

Continuous line: regression curve of experimental data; squares: simulation results.

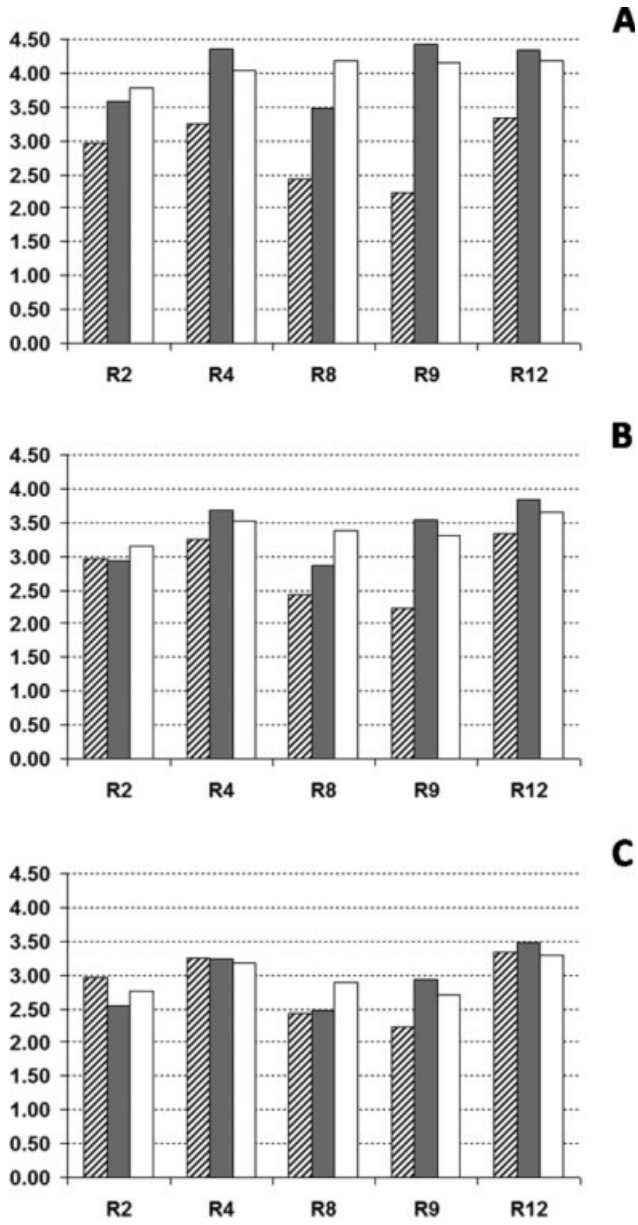

Figure 7. Comparisons between the values predicted and those experimentally measured in two axial planes at 45° between the baffles, in the points indicated as R2, R4, R8, R9, R12 for the d_{32}, for different values of the breakage constant C_1 and for the theoretical coalescence constant C_7; porous sparger reactor, 250 rpm, 0.093 vvm. A: $C_1/C_{1,bf} = 1/3$; B: $C_1/C_{1,bf} = 2/3$; C: $C_1/C_{1,bf} = 1$, where $C_{1,bf}$ is the best fitting value of the constant.

First bar: experimental values, second bar: values predicted on plane at 45°, third bar: values predicted on plane at 135°. Values in mm.

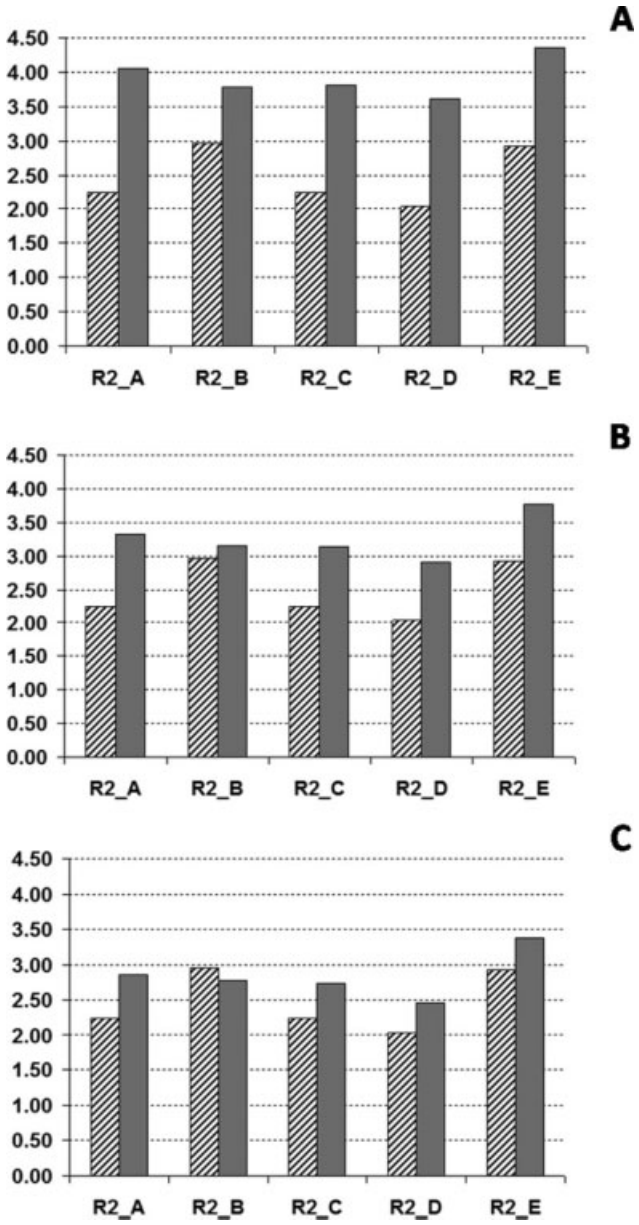

Figure 8. Comparisons between the values predicted and those experimentally measured in the tangential impeller plane in the points R2_A, R2_B, R2_C, R2_D, R2_E for the d_{32}, for different values of the breakage constant C_1 and for the theoretical coalescence constant C_7; porous sparger reactor, 250 rpm, 0.093 vvm. A: $C_1/C_{1,bf} = 1/3$; B: $C_1/C_{1,bf} = 2/3$; C: $C_1/C_{1,bf} = 1$, where $C_{1,bf}$ is the best fitting value of the constant.

First bar: experimental values, second bar: values predicted. Values in mm.

a stirring speed of 250 rpm and a gassing flow rate of 0.093 vvm is reported in Figure 5. In accordance with the empirical correlations,[69–71] the gas is well dispersed in the reactor under these operating conditions, showing local accumulation in the recirculation zones, as it is usually observed experimentally. According to the gassing rate and the stirring

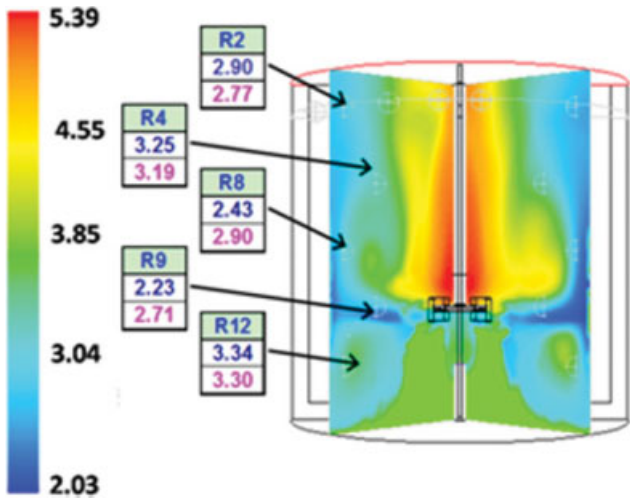

Figure 9. Contour plot of the local d_{32} and comparisons between the values predicted (second row) and those experimentally measured (first row) in two axial planes at 45° between the baffles, in the points indicated as R2, R4, R8, R9, R12, for the best fitting value of the breakage constant C_1 and for the theoretical value of the coalescence constant C_7.

Porous sparger reactor, 250 rpm, 0.093 vvm. Values in mm. [Color figure can be viewed in the online issue, which is available at www.interscience.wiley.com.]

speed different fluid dynamic regimes can be observed behind the stirrer blades, corresponding to different cavity structures. At low gassing rates low gas volume fractions (far lower than one) are observed near the blades, forming the vortex cavity structure. This is the case predicted by this

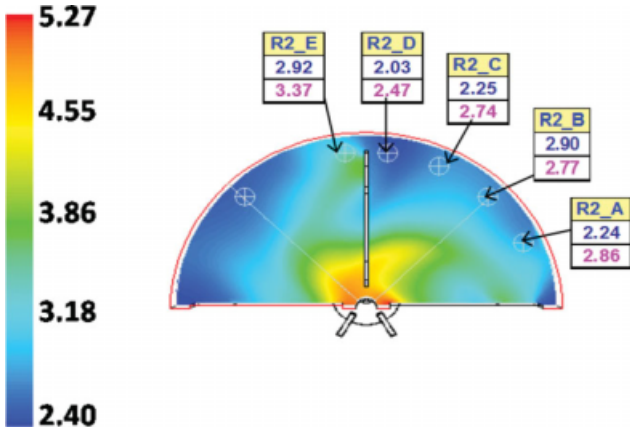

Figure 10. Contour plot of the local d_{32} and comparisons between the values predicted (second row) and those experimentally measured (first row), in the tangential impeller plane in the points R2_A, R2_B, R2_C, R2_D, R2_E, for the best fitting value of the breakage constant C_1 and for the theoretical value of the coalescence constant C_7.

Porous sparger reactor, 250 rpm, 0.093 vvm. Values in mm. [Color figure can be viewed in the online issue, which is available at www.interscience.wiley.com.]

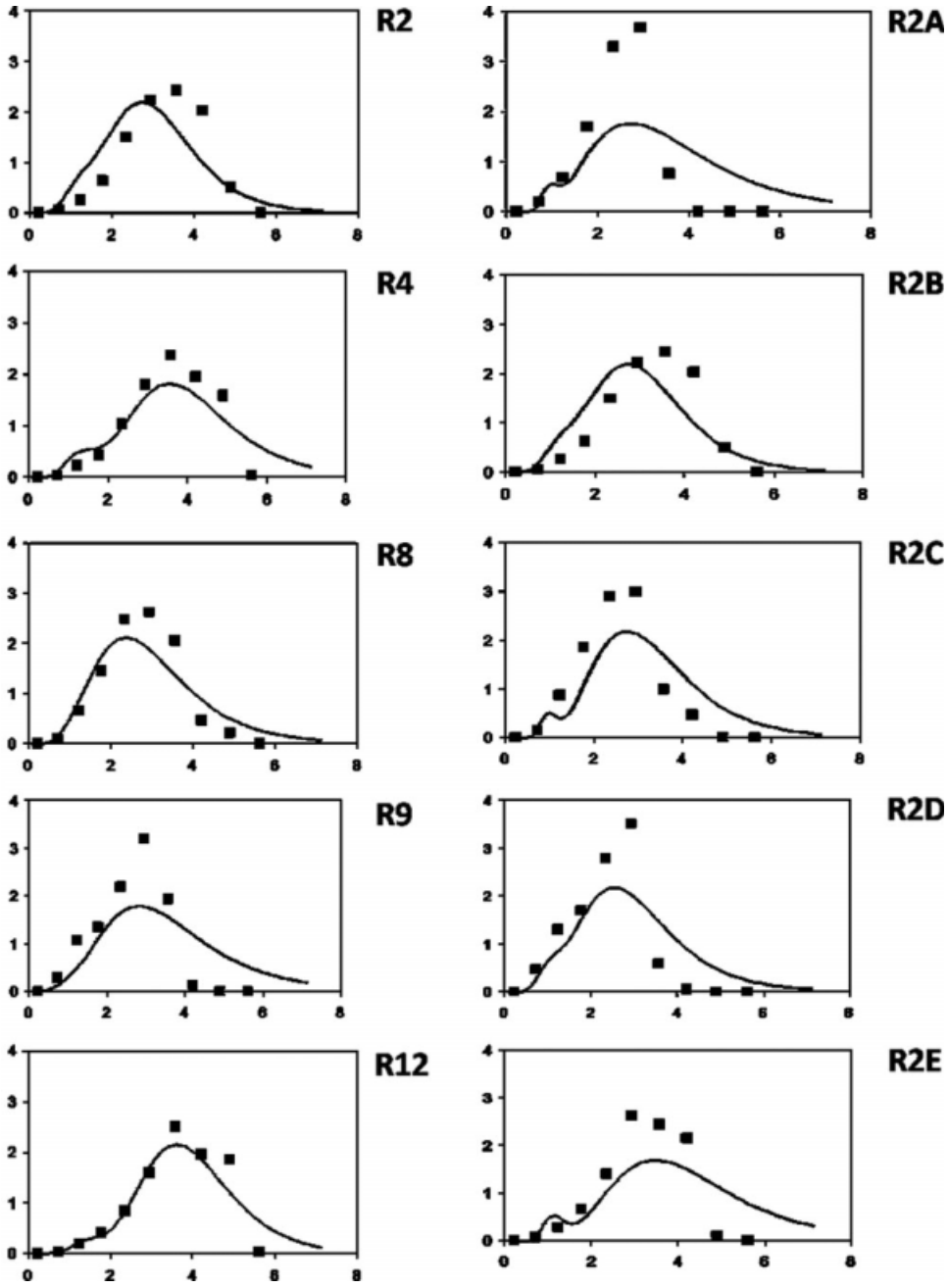

Figure 11. Comparison of the local BSD, reconstructed from the moments (continuous line) and expressed as volume density (dimensionless and scaled by a proper factor),with the experimental one (squares) in the measurement points, for the best fitting value of the breakage constant C_1 and for the theoretical coalescence constant C_7.

Porous sparger reactor, 250 rpm, 0.093 vvm.

simulation, in complete accordance with the empirical correlations for the operating conditions examined (250 rpm, 0.093 vvm).[70]

A comparison of the predicted values for the global hold-up has been possible for the ring sparger reactor for which many experimental data were available,[45,46] for a wide range of operating conditions, up to global hold-up values of about 7%. The comparison is reported in Figure 6 and as it is seen the predicted global hold-up values agree better with the experimental ones at intermediate and higher gassing rates; the simulation results are not reported for flow rates falling in the range between 0.1 and 0.4 vvm, since gas cavities undergo the transition from the vortex structure to the large cavity structure, and the MRF fails to describe this transient and unstable regime.

The final CFD model contained a single parameter that could not be determined directly from theoretical calculations: the break-up constant C_1 reported in Eq. 20.

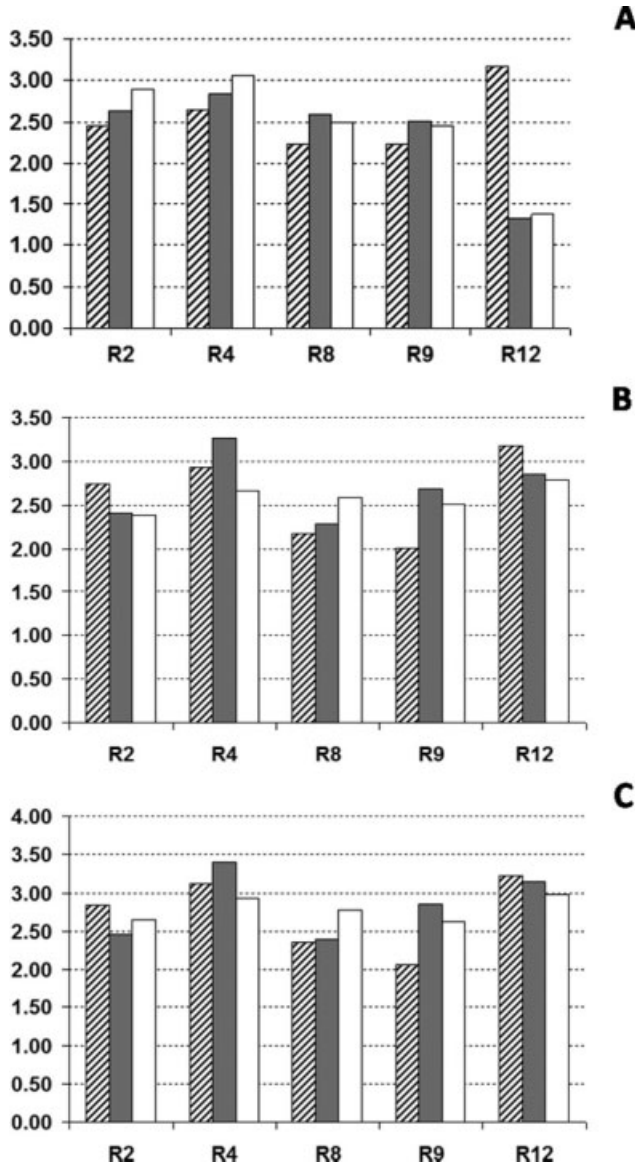

Figure 12. Comparisons between the values predicted and those experimentally measured in two axial planes at 45° between the baffles, in the points indicated as R2, R4, R8, R9, R12 for the d_{32}, for different operating conditions; for the best fitting value of the breakage constant C_1 and the theoretical value of the coalescence constant C_7; porous sparger reactor. A: 157 rpm, 0.052 vvm; B: 250 rpm, 0.052 vvm; C: 250 rpm, 0.072 vvm.

First bar: experimental values, second bar: values predicted on plane at 45°, third bar: values predicted on plane at 135°. Values in mm.

Therefore, as a first step of this work a number of simulations, for the porous sparger configuration, were performed by employing different break-up values and model predictions were compared with experimental data for the mean bubble size in the different spatial locations, and under different operating conditions (i.e., gassing and stirring rates) in order to verify the best fitting value of the constant $C_{1,bf}$.

An example of this sensitivity analysis is reported in Figures 7 and 8 and for a stirring rate of 250 rpm and a gassing rate of 0.093 vvm. Figure 7 compares model predictions in two planes (at 45° and 135°) with the experimental measurements in R2, R4, R8, R9, R12 for three different values of

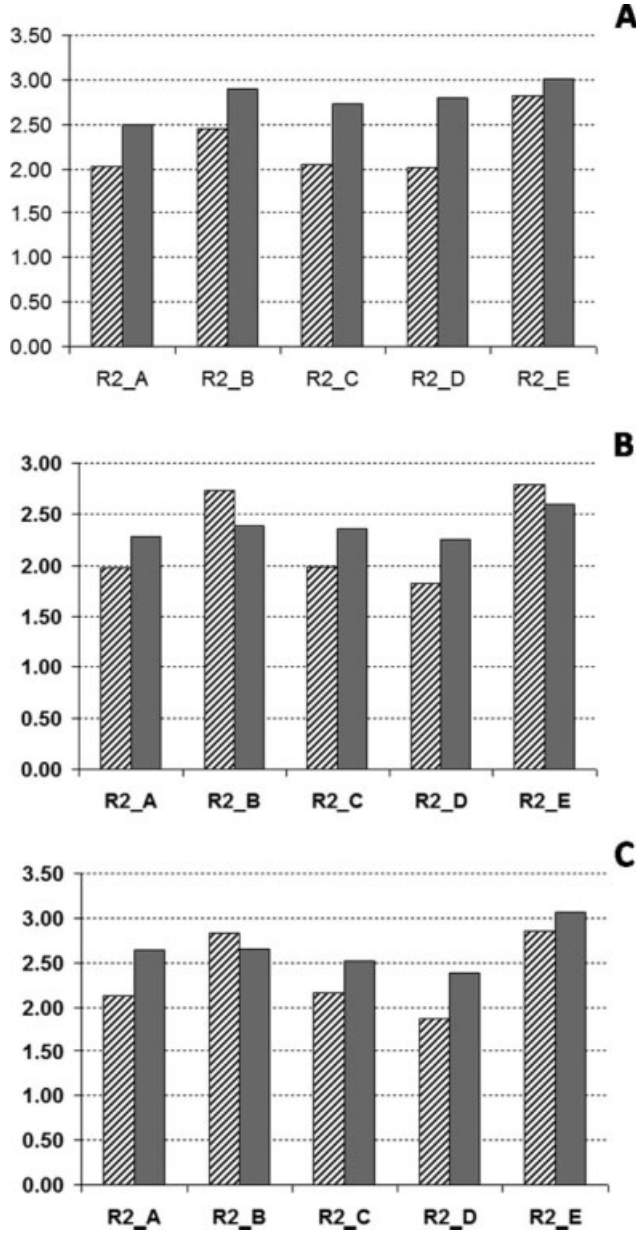

Figure 13. Comparisons between the values predicted and those experimentally measured in the tangential impeller plane in the points R2_A, R2_B, R2_C, R2_D, R2_E for the d_{32}, for different operating conditions; for the best fitting value of the breakage constant C_1 and the theoretical value of the coalescence constant C_7; porous sparger reactor. A: 157 rpm, 0.052 vvm; B: 250 rpm, 0.052 vvm; C: 250 rpm, 0.072 vvm.

First bar: experimental values, second bar: values predicted. Values in mm.

the break-up constant, corresponding to one third and two third of the best fitting value and for the best fitting value itself. As expected, a progressive reduction of the local mean diameters is observed as the value of the break-up constant increases and, the best agreement is obtained for $C_1 = C_{1,bf}$. Comparison for values of C_1 bigger than the best fitting value (not reported for the sake of brevity) resulted in worse agreement with experimental data. The same comparison for the same three values of C_1 is reported in Figure 8 for R2_A, R2_B, R2_C, R2_D, R2_E.

Also simulations performed under different operating conditions (the ones reported in Tables 3 and 4) resulted in the best agreement for $C_1 = C_{1,bf}$ and in what follows only results obtained with this value of the constant will be discussed.

Figures 9 and 10 compare model predictions with experimentally measured mean bubble size, again for a stirring speed of 250 rpm, a gassing rate of 0.093 vvm, for the porous sparger. The agreement is quite good; in the stirrer plane coalescence is observed down wind of baffles (R2_E) due to stationary vortices, whereas break-up prevails up wind of baffles (R2_D) owing to the higher turbulent dissipation rate.

The detailed comparison between the measured (symbols) and the predicted (continuous line) local BSDs in the 10 measuring points for these operating conditions is reported in Figure 11. The measuring locations lay in two meridian planes at 45° between the baffles, in the points indicated as R2, R4, R8, R9, R12 and in the tangential impeller plane, in the points R2_A, R2_B, R2_C, R2_D, R2_E (Figures 9 and 10). The reconstruction of the local predicted BSD from the computed moments has been performed assuming a BSD given by the sum of two log-normal distributions, whose parameters have been evaluated from the six moments, and then compared with the experimental distributions in terms of volume densities.

On the whole, the model is able to describe qualitatively and quantitatively the experimental trend of bubbles diameters in the measurement points. The smaller bubbles are located in the stream exiting from the impeller (R9), where

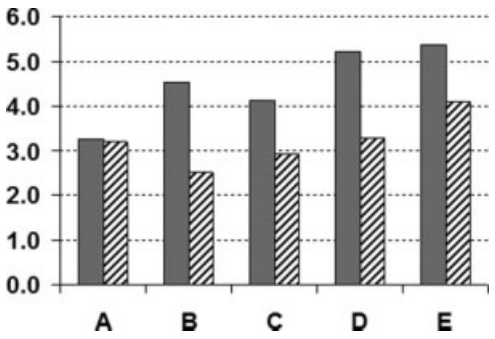

Figure 14. Comparison of the d_{32} predicted and that experimentally measured in an axial plane at 45° between the baffles, in the points indicated as A, B, C, D, E in the paper by Laakkonen et al.[53] Ring sparger reactor, 390 rpm, 0.7 vvm.

First bar: values predicted, second bar: experimental values. Values in mm.

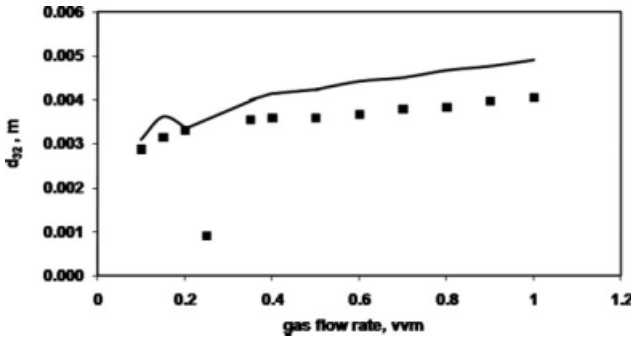

Figure 15. Comparison of the mean value of d_{32} in the reactor predicted by the simulation (continuous line) and that found by Calderbank's empirical relation[57] (squares).

Ring sparger reactor, 390 rpm,different gassing rates.

turbulence is higher and the effect of break-up is more intense. On the contrary the largest ones are in the recirculation zones (R4, R12), where coalescence prevails. However, when it comes to the detailed comparisons of the BSD, it is clearly evident that the predicted BSDs are characterized by longer tails with respect to the experimental ones (highlighting a possible underestimation of higher order moments).

Similar trends were observed for the other operating conditions reported in Table 3 as well. For example, the comparison between predicted and experimentally measured mean bubble size at different stirring and gassing rates [i.e., 157 rpm and 0.052 vvm (A), 250 rpm and 0.052 vvm (B), 250 rpm and 0.072 vvm (C)] is reported in Figure 12 for five different measurement points (R2, R4, R8, R9, R12) and is reported in Figure 13 for five other points (R2_A, R2_B, R2_C, R2_D, R2_E). As it is clearly seen, good agreement was observed also under these operating conditions.

For the reactor operating with the ring sparger the only detailed comparison for the experimental BSDs was possible at 390 rpm and 0.7 vvm, still giving a satisfactory agreement, as shown in Figure 14, where the comparison in five different points (labelled as A, B, C, D, E, as indicated also in Figure 3b) is reported. The simulation was performed by using the same set of coalescence and break-up constants as used for the porous sparger, although the flow rate is now eight times bigger.

For the other operating conditions reported in Table 4 no experimental data concerning the mean bubble size were available, therefore, model predictions were compared with the values given by the Calderbank correlation.[72] The comparison for the mean value of the Sauter diameter throughout the entire reactor, for a stirring rate of 390 rpm at different gassing rates (ranging from 0.1 to 1 vvm) is reported in Figure 15, resulting again in satisfactory agreement.

Conclusions

In this work, an approach for the simulation of stirred gas–liquid reactors that couples CFD and PBM is proposed and discussed. The population balance is solved by resorting to QMOM and considers the effects of coalescence and break-up on the BSD. The flow field is described with a

two-fluid Eulerian-Eulerian model under some simplification hypotheses. In fact, a uniform bubble terminal velocity was considered, and the drag force was evaluated on the basis of the local mean Sauter diameter (rather than the entire BSD).

The spatial discretisation procedure of the transport equations may lead to the corruption of the moment sets generating nonphysical results, and, thus, an algorithm for their correction has been devised and implemented. This correction method was found to play a crucial role both in term of the numerical stability of the simulation and the physical consistency of the results.

The approach was tested under a wide range of operating conditions (sparger design, stirrer speed, gas flow rate, with global hold ups ranging from 0.2 to 7%) and resulted in accurate predictions for both the local gas distribution and the global hold up.

It is worth noticing that the coalescence and break-up kernels used in the population balance mainly include constants that were determined from first principles and only one constant was left to be identified from fitting with experiments. Nevertheless, the modeling approach with a unique set of coalescence and break-up constants was capable of reproducing satisfactorily the experimental BSDs under very different operating conditions and for two different reactor configurations.

Notation

$\mathbf{a}_0$ = initial vector of third order differences
$\mathbf{a}_1$ = final vector of third order differences
$\mathbf{b}_k$ = response vector describing the change of the vector of the third order differences to a unit increment in the moment $\ln m_k$
$B(L; x, t)$ = birth rate of bubbles with size L
$B^B(L)$ = birth rate due to breakage
$B^C(L)$ = birth rate due to coalescence
$\overline{B}_k$ = birth rate of moment of order k
c_k = multiplicative constant for the change of moment m_k
C_i = constants of the kernel of breakage (i = 1, 2, 3) or of coalescence (i = 7, 8)
C_D = drag coefficient
C_μ = constant of the turbulent model
$C_{1\varepsilon}$ = constant of the turbulent model
$C_{2\varepsilon}$ = constant of the turbulent model
$D(L; \mathbf{x}, t)$ = death rate of bubbles with size L
$D^B(L)$ = death rate due to breakage
$D^C(L)$ = death rate due to coalescence
$\overline{D}_k$ = death rate of moment of order k
d_b = bubble diameter
$d_{b,inlet}$ = bubble diameter at the inlet
d_p = diameter of sparger pore
d_s = sparger diameter
d_{32} = bubble Sauter diameter
$\mathbf{F}_{cd}$ = interphase force due to drag
Fr = Froude number
$\mathbf{g}$ = gravitational acceleration
G_k = production of turbulent kinetic energy
$g(L)$ = breakage kernel
k = turbulent kinetic energy
k_V = volume shape factor
$h(L, \lambda)$ = coalescence kernel
k_A = area shape factor
L = bubble size
L_i = node of the quadrature approximation
m_k = moment of order k of the BSD
N_d = number of nodes of the quadrature approximation
N_T = total number of bubbles per unit volume
$n(L;\mathbf{x},t)$ = bubble number density function
p = pressure shared by the two phases
Re = Reynolds number
$\overline{S}_k$ = global source term for moment of order k
$S^k_{\phi_d}$ = fluent user defined scalar source term in the dispersed phase
t = time
$\mathbf{T}_c$ = stress strain tensor for the continuous phase
$\mathbf{T}_d$ = stress strain tensor for the disperse phase
$\mathbf{T}_k$ = stress strain tensor for a generic phase k
$\overline{\mathbf{U}}_c$ = time–averaged velocity of the continuous phase
$\overline{\mathbf{U}}_d$ = time–averaged velocity of the disperse phase
$\overline{\mathbf{U}}_k$ = time–averaged velocity of a generic phase k
$\overline{\mathbf{U}}^k_d$ = time–averaged velocity of the moment of order k
$\overline{\mathbf{U}}_m$ = time–averaged averaged velocity of the mixture
U_∞ = bubble terminal velocity
$\mathbf{x}$ = position vector
x_1 = first coordinate of the position vector
x_2 = second coordinate of the position vector
x_3 = third coordinate of the position vector
We = Weber number
w_i = weight of the quadrature approximation

Greek letters

α_c = volume fraction of the continuous liquid phase
α_d = volume fraction of the dispersed gas bubble phase
$\beta(L, \lambda)$ = daughter distribution function
Γ^k_d = diffusivity of fluent user defined scalar associated to the disperse phase
λ = bubble size
ε = turbulence dissipation rate
μ = mean of the distribution
μ_{air} = molecular viscosity of air
μ_c = molecular viscosity of the continuous phase
μ_t = turbulent viscosity of the mixture
$\mu_{t,c}$ = turbulent viscosity of the continuous phase
$\mu_{t,d}$ = turbulent viscosity of the disperse phase
μ_k = molecular viscosity of a generic phase k
$\mu_{t,k}$ = turbulent viscosity of a generic phase k
μ_{water} = molecular viscosity of water
$\eta(\lambda,L)$ = coalescence efficiency
ρ_{air} = density of air
ρ_c = time averaged density of the continuous liquid phase
ρ_d = time averaged density of the disperse phase
ρ_m = density of the mixture
ρ_{water} = density of water
σ = surface tension
σ = variance of the distribution
σ_k = constant of the turbulent model
σ_ε = constant of the turbulent model
ϕ^k_d = fluent user defined scalar associated to the disperse phase

Literature Cited

1. Lane GL. *Computational modeling of gas-liquid flow in stirred tanks*. PhD Dissertation, University of Newcastle, Australia, 2006.
2. Gimbun J, Rielly CD, Nagy ZK. Modeling of mass transfer in gas-liquid stirred tanks agitated by Rushton turbine and CD-6 impeller: a scale-up study. *Chem Eng Res Des*. 2009;87:437–451.
3. Harvey PS, Greaves M. Turbulent flow in an agitated vessel. I. Predictive Model. *Trans I. Chem. E*. 1982;60:195–210.
4. Placek J, Tavlarides LL, Smith GW, Fort I. Turbulent flow in stirred tanks. II. A two-scale model of turbulence. *AIChE J*. 1986;31:1113–1120.
5. Pericleous KA, Patel MK. The source-sink approach in the modeling of stirred reactors. *Phys Chem Hydrodynamics*. 1987;9:279–297.
6. Brucato A, Ciofalo M, Grisafi F, Rizzuti L. Application of a numerical fluid dynamics software to stirred tanks modelling. In: Laforenza D, Perego R, editors. *Supercomputing Tools for Science and Engineering*. Milan: Franco Angeli, 1989:413–419.
7. Brucato A, Ciofalo M, Grisafi F, Rizzuti L. Computer simulation of turbulent fluid flow in baffled and unbaffled tanks stirred by radial

impellers. *Proceedings of International Conference on Computer Applications to Batch Processes*, Cengio, Italy, 1990:69–86.
8. Gosman AD, Lekakou C, Politis S, Issa RI, Looney MK. Multidimensional modeling of turbulent two-phase flows in stirred vessels. *AIChE J*. 1992;38:1946–1956.
9. Ranade VV, Joshi JB, Marathe AG. Flow generated by pitched blade turbines. II. Simulation using k-ε model. *Chem Eng Commun*. 1989;81:225–248.
10. Ranade VV, Joshi JB. Flow generated by a disc turbine. II. Mathematical modelling and comparison with experimental data. *Trans IchemE*. 1990;68 (Part A):34–50.
11. Kresta SM, Wood PE. Prediction of the three-dimensional turbulent flow in stirred tanks. *AIChE J*. 1991;37:448–460.
12. Tabor G, Gosman AD, Issa RI. Numerical simulation of the flow in a mixing vessel stirred by a rushton turbine. *IChemE Symp Ser*. 1996;140:25–34.
13. Wechsler K, Breuer M, Durst F. Steady and unsteady computations of turbulent flows induced by a 4/45° pitched blade impeller. *J Fluids Eng*. 1999;121:318–329.
14. Luo JY, Issa RI, Gosman AD. Prediction of impeller-induced flows in mixing vessels using multiple frames of reference. *IchemE Symp Ser*. 1994;136:549–556.
15. Gosman AD, Lekakon C, Politisi S, Issa RI, Looney MK. Multidimensional modeling of turbulent two-phase flow is stirred vessels. *AIChE J*. 1991;38:1946–1956.
16. Trägårdh C. A hydrodynamic model for the simulation of an aerated agitated fed-batch fermenter. *Proceedings of 2nd International Conference on Bioreactor Fluid Dynamics*, Cambridge, UK, September 21, 1988;23:117–134.
17. Ahlstedt H, Lahtinen M. Calculation of flow field in a stirred tank with Rushton turbine impeller. *Proceedings of the third CFX International Users Conference*, Chesham, UK, 30 October-November 1996:91–108.
18. Jaworski Z, Dyster KN, Moore IPT, Nienow AW, Wyszynski ML. The use of angle resolved LDA data to compare two differential turbulence models applied to sliding mesh CFD flow simulations in a stirred tank. *Récents Progrès en Genie des Procédès*. 1997;11:187–194.
19. Sun H, Mao ZS, Yu G. Experimental and numerical study of gas hold-up in surface aerated stirred tanks. *Chem Eng Sci*. 2006;61:4098–4110.
20. Wang W, Mao ZS, Yang C. Experimental and numerical investigation on gas holdup and flooding in an aerated stirred tank with Rushton impeller. *Ind Eng Chem Res*. 2006;45:1141–1151.
21. Bartels C, Breuer M, Wechsler K, Durst F. Computational fluid dynamics applications on parallel-vector computers: computations of stirred vessel flows. *Comput Fluids*. 2002;31:69–97.
22. Derksen J, van den Akker HEA. Large eddy simulations on the flow driven by a Rushton turbine. *AIChE J*. 1999;45:209–221.
23. Hartmann H, Derksen JJ, Montavon C, Pearson J, Hamill IS, van den Akker HEA. Assessment of large eddy and RANS stirred tank simulations by means of LDA. *Chem Eng Sci*. 2004;59:2419–2432.
24. Bakker A. *Hydrodynamics of stirred gas-liquid dispersions*. Ph.D. Thesis, Technical University of Delft, The Netherlands, 1992.
25. Brucato A, Ciofalo M, Grisafi F, Micale G. Numerical prediction of flow fields in baffled stirred vessels: a comparison of alternative modeling approaches. *Chem Eng Sci*. 1998;53:3653–3684.
26. Aubin J, Fletcher DF, Xuereb C. Modeling turbulent flow in stirred tanks with CFD: the influence of the modeling approach, turbulence model and numerical scheme. *Exp Therm Fluid Sci*. 2004;28:431–445.
27. Luo JY, Gosman AD, Issa RI, Middleton JC, Fitzgerald MK. Full flow field computation of mixing baffled stirred vessels. *Chem Eng Res Des*. 1993;71 (Part A):342–344.
28. Deen NG, Solberg T, Hjertager BH. Flow generated by an aerated Rushton impeller: two-phase PIV experiments and numerical simulations. *Can J Chem Eng*. 2002;80:638–652.
29. Scargiali F, D'Orazio F, Grisafi F, Brucato A. Modelling and simulation of gas-liquid hydrodynamics in mechanically stirred tanks. *Chem Eng Res Des*. 2007;85:637–646.
30. Bakker A, van den Akker HEA. A computational model for the gas-liquid flow in stirred reactors. *Chem Eng Res Des Trans IchemE*. 1994;72 (Part A):594–606.
31. Lane GL, Schwarz MP, Evans GM. Numerical modelling of gas-liquid flow in stirred tanks. *Chem Eng Sci*. 2005;60:2203–2214.
32. Djebbar R, Roustan M, Line A. Numerical computation of turbulent gas-liquid dispersion in mechanically agitated vessels. *Chem Eng Res Des*. 1996;74 (Part A):492–498.
33. Lane GL, Schwarz MP, Evans GM. Predicting gas-liquid flow in a mechanically stirred tank. *Appl Math Model*. 2002;2:223–235.
34. Kerdouss F, Bannari A, Proulx P. CFD modelling of gas dispersion and bubble size in a double turbine stirred tank. *Chem Eng Sci*. 2006;61:3313–3332.
35. Moilanen P, Laakkonen M, Visuri O, Alopaeus V, Aittamaa J. Modeling mass transfer in an aerated 0.2 m^3 vessel agitated by Rushton, Phasejet, and Combijet impellers. *Chem Eng J*. 2008;142:95–108.
36. Muhr H, David R, Villermaux J. Crystallization and precipitation engineering. VI. Solving population balance in the case of the precipitation of silver bromide crystals with high primary nucleation rates by using the first order upwind differentiation. *Chem Eng Sci*. 1996;51:309–319.
37. Vanni M. Approximate population balance equations for aggregation-breakage processes. *J Colloid Interface Sci*. 2000;221:143–160.
38. Venneker BCH, Derksen JJ, Van den Akker HEA. Population balance modeling of aerated stirred vessels based on CFD. *AIChE J*. 2002;48:673–685.
39. Montante G, Horn D, Paglianti A. Gas-liquid flow and bubble size distribution in stirred tanks. *Chem Eng Sci*. 2008;63:2107–2118.
40. Kerdouss F, Bannari A, Proulx P, Bannari R, Skrga M, Labrecque Y. Two-phase mass transfer coefficient prediction in stirred vessel with a CFD model. *Comput Chem Eng*. 2008;32:1943–1955.
41. Hulburt HM, Katz S. Some problems in particle technology. A statistical mechanical formulation. *Chem Eng Sci*. 1964;19:555–574.
42. Marchisio DL, Barresi AA, Garbero M. Nucleation, growth, and agglomeration in barium sulfate turbulent precipitation. *AIChE J*. 2002;48:2039–2050.
43. McGraw R. Description of aerosol dynamics by the quadrature method of moments. *Aerosol Sci Technol*. 1997;27:255–265.
44. Marchisio DL, Vigil RD, Fox OD. Quadrature method of moments for aggregation-breakage processes. *J Colloid Interface Sci*. 2003;258:322–334.
45. Laakkonen M, Alopaeus V, Aittamaa J. Validation of bubble breakage, coalescence and mass transfer models for gas-liquid dispersion in agitated vessel. *Chem Eng Sci*. 2006;61:218–228.
46. Laakkonen M, Moilanen P, Alopaeus V, Aittamaa J. Modeling local bubble size distributions in agitated vessels. *Chem Eng Sci*. 2007;62:721–740.
47. McGraw R. Correcting moment sequences for errors associated with advective transport. 2006. Available at: http://www.ecd.bnl.gov/pubs/momentcorrection_mcgraw2006.pdf
48. Wright DL. Numerical advection of moments of the particle size distribution in Eulerian models. *J Aerosol Sci*. 2007;38:352–369.
49. Spalding DB. Computer simulation of two-phase flows with special reference to nuclear reactor systems. In: Lewis RW, Morgan K, Johnson JA, Smith WR, editors. *Computational Techniques in Heat Transfer*. Swansea: Pineridge Press, 1985:1–44.
50. Petitti M, Caramellino M, Marchisio DL, Vanni M. Two-scale simulation of mass transfer in an agitated gas-liquid tank. *Proceedings of International Conference on Multiphase Flows, ICMF 2007*, Leipzig, Germany, 9–13 July 2007, paper S6_Tue_A_16.
51. Petitti M, Marchisio DL, Vanni M, Baldi G, Mancini N, Podenzani F. Effect of drag modeling on the prediction of critical regime transitions in agitated gas-liquid reactors with bubble size distribution modelling. *Multiphase Sci Technol*. 2009;21:1–12.
52. Ishii M, Zuber N. Drag coefficient and relative velocity in bubbly, droplet or particulate flows. *AIChE J*. 2002;45:707–721.
53. Tomiyama A. Drag, lift and virtual mass forces acting on a single bubble. *3rd International Symposium Two-Phase. Flow Mod Exp*. 22–24 September 2004, Pisa, Italy.
54. Fox RO. Introduction and fundamentals of modeling approaches for polydisperse multiphase flows. In: Marchisio DL, Fox RO, editors. *Multiphase Reacting Flows: Modelling and Simulation*. Wien: Springer Verlag, CISM Series, 2007;492:1–40.
55. Narsimhan G, Gupta JP, Ramkrishna D. A model for transitional breakage probability of droplets in agitated lean liquid-liquid dispersions. *Chem Eng Sci*. 1979;34:257–265.
56. Alopaeus V, Koskinen J, Keskinen KI, Majander J. Simulation of the population balances for liquid-liquid systems in a non ideal

stirred tank. II. Parameter fitting and the use of the multiblock model for dense dispersions. *Chem Eng Sci*. 2002;57:1815–1825.
57. Andersson R, Andersson B. On the breakup of fluid particles in turbulent flows. *AlChE J*. 2006;52:2020–2030.
58. Coulaloglou CA, Tavlarides LL. Description of interaction processes in agitated liquid-liquid dispersions. *Chem Eng Sci*. 1977;32:1289–1297.
59. Prince MJ, Blanch HW. Bubble coalescence and break-up in air-sparged bubble columns. *AIChE J*. 1990;36:1485–1499.
60. Tsouris C, Tavlarides LL. Breakage and coalescence models for drops in turbulent dispersions. *AIChE J*. 1994;40:395–406.
61. Alopaeus V, Koskinen J, Keskinen K. Simulation of the population balances for liquid-liquid systems in a nonideal stirred tank. I. Description and qualitative validation of the model. *Chem Eng Sci*. 1999;54:5887–5899.
62. Gordon RG. Error bounds in equilibrium statistical mechanics. *J Math Phys*. 1968;9:655–667.
63. Marchisio DL. Quadrature method of moments for poly-disperse flows. In: Marchisio DL, Fox RO, editors. *Multiphase Reacting Flows: Modeling and Simulation*. Wien: Springer Verlag, CISM Series, 2007;492:41–77.
64. Shohat JA, Tamarkin JD. *The Problem of Moments*. Providence, RI: American Mathematical Society, 1943.
65. Clift R, Grace JR, Weber ME. *Bubbles, Drops Particles*. New York, San Francisco, London: Academic Press Inc, 1978:172.
66. Montante G, Paglianti A, Magelli F. Experimental analysis and computational modelling of gas-liquid stirred vessels. *Trans Inst Chem Eng*. 2007;85:647–653.
67. Kazakis NA, Mouza AA, Paras SV. Experimental study of bubble formation at metal porous spargers: effect of liquid properties and sparger characteristics on the initial bubble size distribution. *Chem Eng J*. 2008;137, 2:265–281.
68. Geary NW, Rice RG. Bubble size prediction for rigid and flexible spargers. *AlChE J*. 1991;37:161–168.
69. Nienow AW, Wisdom DJ, Middleton JC. The effect of scale and geometry on flooding, recirculation and power in gassed stirred vessels. *Proceedings of the 2nd European Mixing Conference*, Cambridge. 1977:17–34.
70. Bombac A, Zun I, Filipic B. Gas-filled cavity structures and local void fraction distribution in aerated stirred vessel. *AlChE J*. 1997;43:2921–2931.
71. Gezork,KM, Bujalski W, Cooke M, Nienow AW. The transition from homogeneous to heterogeneous flow in a gassed stirred vessel. *Trans Inst Chem Eng*. 2000;78 (Part A):363–370.
72. Calderbank PH. Physical rate processes in industrial fermentation. I. The interfacial area in gas-liquid contacting with mechanical agitation. *Trans Inst Chem Eng*. 1958;36:443–463.

Appendix A

The validity of the moment set can be verified by calculating a difference table of the function $\ln(m_k)$. In the first column the sequence of moments, in ascending order, is reported. In the next column the differences between two neighbouring elements, sitting in the same precedent column and in two subsequent rows, are reported. The procedure is continued until a zero appears in the first row. The values reported in the different columns represent the second, third and higher-order differences vectors of the function $\ln(m_k)$. If a moment m_k is changed as follows:

$$(m_k)_1 = c_k(m_k)_0, \tag{A1}$$

its natural logarithm undergoes the following change:

$$\ln(m_k)_1 = \ln c_k + \ln(m_k)_0, \tag{A2}$$

where $\ln(m_k)_0$ is its initial value and $\ln(m_k)_1$ its final value. The consequent variation in the third order differences vector, that is to say the vector whose magnitude is given by the sum of the squares of the elements of the second order differences (elements of column d_2 of Tables 1 and 2), results in:

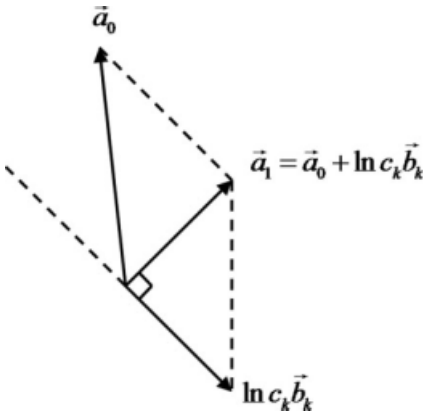

Figure A1. Variation of the vector of third order differences due to moment correction.

$$\mathbf{a}_1 - \mathbf{a}_0 = \ln c_k \mathbf{b}_k, \tag{A3}$$

where $\mathbf{a}_0$ and $\mathbf{a}_1$ are respectively the initial and final vectors of third order differences, while $\mathbf{b}_k$ is the response vector describing the change of the vector of the third order differences to a unit increment in $\ln(m_k)$. Thus the final vector is:

$$\mathbf{a}_1 = \mathbf{a}_0 + \ln c_k \mathbf{b}_k \tag{A4}$$

This vector presents a minimum length when it results orthogonal to the vector $\mathbf{b}_k$, as shown in Figure A1.

$$(\mathbf{a}_0 + \ln c_k \mathbf{b}_k) \cdot \mathbf{b}_k = 0 \tag{A5}$$

The value of c_k through which $\mathbf{a}_1$ is minimized is thus obtained by the following relationship:

$$\ln c_k = -\cos(\mathbf{a}_0, \mathbf{b}_k) \frac{|\mathbf{a}_0|}{|\mathbf{b}_k|} = -\frac{(\mathbf{a}_0 \cdot \mathbf{b}_k)}{|\mathbf{b}_k|^2}. \tag{A6}$$

The resulting minimum squared amplitude results in:

$$|\mathbf{a}_1|^2 = |\mathbf{a}_0 + \ln c_k \mathbf{b}_k|^2 = |\mathbf{a}_0|^2 \left[1 - \cos^2(\mathbf{a}_0, \mathbf{b}_k)\right]. \tag{A7}$$

In the correction algorithm the choice of the index of the moment to correct is chosen with the objective of achieving the maximum smoothness for the function $\ln(m_k)$. Thus it is chosen the moment with the correction of which the third order differences vector is minimized. Thus the index k^* of the moment that must be corrected is chosen as the one that gives gives the largest $\cos^2(\mathbf{a}_0, \mathbf{b}_k)$, for any moment of index k.

The entity of the correction is given by the orthogonality relation, always with the purpose of minimizing the final vector and reaching the maximum smoothness, resulting in the following equation:

$$\ln c_k = -\cos(\mathbf{a}_0, \mathbf{b}_{k^*}) \frac{|\mathbf{a}_0|}{|\mathbf{b}_{k^*}|} = -\frac{(\mathbf{a}_0 \cdot \mathbf{b}_{k^*})}{|\mathbf{b}_{k^*}|^2}. \tag{A8}$$

Appendix B

The second correction algorithm consists in calculating the new set of moments as the arithmetic mean of those corresponding to two log-normal distributions. A log-normal distribution has the following functional form:

$$n(L) = N_T \frac{\exp\left[\frac{-(\ln L-\mu)^2}{2\sigma^2}\right]}{L\sigma\sqrt{2\pi}}, \tag{B1}$$

corresponding to the following generic moment m_k:

$$m_k = N_T \exp\left(k\mu + \frac{k^2\sigma^2}{2}\right), \tag{B2}$$

where N_T is the total number of bubbles per unit volume, μ is the mean bubble size, whereas σ is the variance of the distribution. The three parameters for the first distribution are calculated by forcing only m_0, m_1, m_3 to be equal to those of the original set of moments, whereas the three parameters of the second distribution are calculated by forcing m_0, m_2, m_3.

Appendix C

In Fluent it is possible to solve additional transport equations through User-Defined Scalars. The equation for a generic scalar ϕ_d^k associated to the dispersed phase is:

$$\frac{\partial \alpha_d \rho_d \phi_d^k}{\partial t} + \nabla \cdot \left(\alpha_d \rho_d \overline{\mathbf{U}}_d \phi_d^k\right) - \nabla \cdot \left(\alpha_d \rho_d \Gamma_d^k \nabla \cdot \phi_d^k\right) = \rho_d \alpha_d S_{\phi_d}^k, \tag{C1}$$

By neglecting the diffusive transport, by defining each scalar as follows:

$$\phi_d^k = \frac{m_k}{\alpha_d}, \tag{C2}$$

and by considering $\alpha_d S_{\phi_d}^k$ as the moment source term, it is possible to obtain from Eq. C1 the moment transport equation reported in Eq. 26.

The source terms $\bar{\rho}_d S_k$ for the different moments are calculated and returned by a proper user-defined function in which the nodes and the weights of the quadrature approximation are evaluated, after the possible correction of the moment set.

Manuscript received Dec. 5, 2008, and revision received May 14, 2009.